

# Ridged twin boundaries as prolific dislocation sources in high-entropy alloys and other low stacking-fault energy metals

Qian Yu (✉ [yu\\_qian@zju.edu.cn](mailto:yu_qian@zju.edu.cn))

Zhejiang University <https://orcid.org/0000-0003-4413-9744>

Xiaoqian Fu

Zhejiang University

Jun Ding

Xi'an Jiaotong University <https://orcid.org/0000-0002-4091-8663>

Cigdem Ozsoy-Keskinbora

Thermo Fisher Scientific

Guang Yang

Thermo Fisher Scientific Inc.

Yujie Chen

Zhejiang University

Yan Fang

Zhejiang University

Eun Soo Park

Seoul National University <https://orcid.org/0000-0001-8520-2012>

Ze Zhang

Zhejiang University

Robert Ritchie

University of California Berkeley <https://orcid.org/0000-0002-0501-6998>

En Ma

Xi'an Jiaotong University <https://orcid.org/0000-0002-7468-4340>

---

Physical Sciences - Article

Keywords:

Posted Date: May 25th, 2022

DOI: <https://doi.org/10.21203/rs.3.rs-1477385/v1>

**License:**  This work is licensed under a Creative Commons Attribution 4.0 International License.

[Read Full License](#)

---

# Abstract

Dislocation activities play an important role in mediating plastic deformation, even in metals that are prone to deformation twinning. Combining multi-scale and in situ electron microscope characterizations, here we report a discovery of a unique type of dislocation sources that are particularly fertile in low stacking-fault energy materials, including CrCoNi-based high-entropy alloys and twinning-induced plasticity steel. These sources reside on nano-sized ridges, which form strings along the borders between different twin variants to accommodate the multiple twinning relationships. Upon plastic deformation, such ridge-twin structures act as an effective dislocation generator, from which dislocations are emitted into the coherent twin boundaries or cross slip into the interior of grains. At larger strain, the incoherent boundaries of the nano-sized ridge-twins emit partial dislocations to mediate deformation twinning as well. Molecular dynamic simulations indicate that the formation of nano-sized ridge-twin structures is energetically favorable at the junctions between multiple twins, explaining why such structures are ubiquitously populous in the twinned architectures that are commonplace in the several low stacking-fault energy materials that we investigated. These results shed light on understanding the origin of dislocation plasticity in low stacking-fault energy metals and alloys including those known for twinning-induced plasticity.

# Full Text

Dislocations are the primary structural defect that influences the mechanical behavior of metals. Even for low stacking-fault energy (SFE) materials, including twinning-induced plasticity (TWIP) materials that can acquire significant plastic strain from twinning shear, dislocation slip is still a dominant contributor to their mechanical properties<sup>1-4</sup>. The synergetic effect of dislocation glide and twinning deformation enables low-SFE materials to exhibit a high strain-hardening rate and a good balance of strength and ductility<sup>5-9</sup>. Dislocation slip is also important in facilitating the formation of deformation twins via the pole mechanism<sup>10-12</sup>: the twinning dislocations continue to revolve around the pole dislocation and hence generate layers of stacking faults. In this way, twin embryo nucleates and continuously grows. Moreover, as a special mirror crystal structure that coherently connects with the matrix, deformation twins influence dislocation behavior mainly from two aspects. First, deformation twinning reorients crystal orientations that would be either beneficial or detrimental to dislocation motion<sup>13, 14</sup>. Second, twin boundaries (TBs) hinder dislocations in direct transmission, which contributes to hardening<sup>15-17</sup>.

For low-SFE materials, materials processing such as annealing usually creates twins but can annihilate dislocations. During plastic deformation, dislocations are expected to be generated from boundaries or junctions where the arrangement of atoms is disordered and the local stress concentration is high. However, in materials that easily twin, TBs are usually coherent that rarely induce stress concentration. Therefore, it has been questioned if twins can effectively supply dislocations. When there is a high density of growth twins, such as in nano-twinned materials, grain boundary-twin boundary (GB-TB)

intersections become populous to nucleate dislocations<sup>18-20</sup>. This form of dislocation sources, however, is not prevalent in low-SFE materials in bulk form since their twin density is at least several orders of magnitude lower than that in nano-twinned materials.

Here, we perform multi-scale, three-dimensional and *in situ* electron microscope characterizations on a TWIP high-entropy alloy (HEA), in conjunction with molecular dynamics (MD) simulations, to identify potent dislocation sources in low-SFE materials. We find a category of prolific dislocation sources, namely unique microstructural features that originate from the twin architectures normally expected for low-SFE materials. Specifically, the widespread presence of grains with a twinning relationship leads to strings of nano-sized ridge twins at the twin-twin junctions. These ridges continuously and effectively emit new dislocations. As such, the large number of twin-twin intersections and incoherent twin boundaries (ITBs) act as effective dislocation generators. Molecular dynamics simulations reveal that the formation of such ridge-twin structures are energetically favorable, confirming that they represent a natural consequence of the twin architecture evolution in low-SFE materials.

The material examined in this work is a Cr<sub>20</sub>Mn<sub>14</sub>Fe<sub>26</sub>Co<sub>26</sub>Ni<sub>14</sub> (in at. %) TWIP high-entropy alloy, which was processed in the same way as that described in previous reports<sup>21</sup>. The as-prepared material contains a three-dimensional (3D) twin architecture as a result of the multiple twinning systems, akin to many other low-SFE alloys. In order to obtain a clear view of the twin architecture, we employed focused-ion beam (FIB) - scanning electron beam (SEM) 3D analytical system to examine the microstructure construct in real space. The 3D twin morphology was acquired using the “cut & see” method via continuous cross-sectional observations (sliced in 20 nm increments by FIB and seen by SEM) in a Hitachi NX9000 microscope, in which the FIB system is aligned perpendicular to SEM systems to improve the imaging resolution and avoid any shifts in position.

Extensive annealing twins were observed to intersect with each other in three dimensions within each individual grain. As shown in the SEM images in Fig. 1a, the thickness of the twins ranges from tens of nanometers to micrometers. Each twin contains straight and parallel TBs. Note that at the locations where the multiple twins form junctions, dense and small serrated structures exist along the straight TBs (arrows in red, magnified view in Fig. 1aV). These are strings of triangular structures sandwiched between two different twinned grains (twin variants via different twinning systems). To resolve the crystallography of such triangular structures, we performed scanning transmission electron microscopy (STEM) characterizations under different magnifications. Figure 1b shows a typical low magnification STEM image of this structure, in which we mark Twin1 as T1 and Twin2 as T2. The Matrix-T1 and Matrix-T2 boundaries are straight interfaces, whereas the boundary between T1 and T2 is more complex. The entire T1-T2 boundary is approximately 2 μm long and contains one segment of a ~10 nm long boundary followed by a string of triangular boundaries. The triangles in the string align very well and the size of the triangles varies. The smallest triangle can be as small as only a few nanometers wide.

The microstructure of the boundaries was further investigated under high-resolution STEM mode in the <110> zone axis. The atomic structure is shown in Fig. 1c-g, where all the grain boundaries have

symmetry structures. Technically, Matrix-T1 and Matrix-T2 boundaries are typical  $\Sigma\{111\}$  CTBs (the  $\Sigma$  value represents the reciprocal density of coincidence sites based on the coincident site lattice model<sup>22</sup>). As a  $\Sigma 9$  is created whenever two  $\Sigma 3$ s meet, the T1-T2 boundary is a  $\Sigma 9$  boundary, which is the second most common low- $\Sigma$  boundary in twinning-related grain-boundary engineering<sup>23,24</sup>. Here, the 10 nm long  $\Sigma 9$  boundary is a large-angle grain boundary exhibiting incoherent and symmetry character. Combining with an analysis of the corresponding fast Fourier transform (FFT) image shown in the upper right corner of Fig. 1c, the T1-T2 boundary is characterized as  $\Sigma 9\{114\}$  boundary. The structure of the  $\Sigma 9$  boundary as  $\Sigma 9\{114\}$  only exists in the short length and is soon replaced by the structure containing a string of ridge-shaped nano-twins. From the atomic resolution images (Fig. 1d), it is found that the ridge twins have an identical orientation with matrix in Fig. 1c and show mirror relationships with both T1 and T2, creating special and more interfaces on the  $\Sigma 9$  boundaries including  $\Sigma 3\{111\}$  CTBs,  $\Sigma 3\{112\}$  ITBs, and twin-twin junctions. Importantly, the ridge twin-T1 ITBs display various  $\Sigma 3\{112\}$ -like structures (similar but more complex), as shown in Fig. 1d-g, which are composed of different arrays of Shockley partial dislocations with a sequence different from the exact  $\Sigma 3\{112\}$  structure – b2: b1: b3<sup>25-27</sup>. Some  $\Sigma 3\{112\}$ -like ITBs are dissociated by creating an intrinsic fault on every third  $\{111\}$  plane, with stacking sequence of ...ABC BCA CAB..., the same as a perfect 9R phase<sup>28,29</sup>. The stacking faults within the  $\Sigma 3\{112\}$ -like ITBs are terminated by  $1/6\langle 112 \rangle$  Shockley partial dislocations. Different dislocation configurations result in varying structures. A  $\Sigma 3\{112\}$ -like ITB with obvious deflection accommodated by dislocation structure (as indicated by '^') is shown in Fig. 1g. Due to the different dislocation structures at the  $\Sigma 3\{112\}$ -like ITBs, the shape of the triangular twins also slightly varies from one another. Here, the angles between  $\Sigma 3\{112\}$ -like boundary and  $\Sigma 3\{111\}$  CTBs vary from  $90^\circ$  to  $102^\circ$  with an average of  $98^\circ$ , whereas the typical  $\Sigma 3\{112\}$  ITBs are normal to the  $\Sigma 3\{111\}$  CTBs. Note that the ridged structure is not unique to the HEA under study, but a commonplace feature in the twin architecture of all low-SFE metals and alloys. This is apparent by surveying other low-SFE materials including the equiatomic CrCoNi medium-entropy alloy, TWIP steel, pure Ag and pure Cu, where this type of ridge-twin structures are also common. Typical images of similar ridge-twin structures in different low-SFE materials are shown in Fig. S1 in the Supplementary Information.

To investigate the atomic-scale element distribution on the ridge twin, we performed energy-dispersive X-ray spectroscopy (EDS) mapping in a Spectra Ultra transmission electron microscope (TEM) equipped with UltraX detector. Figure 1h presents the atomic-resolution high-angle annular dark field (HAADF) image and corresponding elemental EDS maps of a ridge twin in the  $\text{Cr}_{20}\text{Mn}_{14}\text{Fe}_{26}\text{Co}_{26}\text{Ni}_{14}$  alloy. The brightness of spots for each EDS map represents the relative concentration of the element in the atomic column along  $\langle 110 \rangle$  zone axis. All the EDS maps show that the element distribution is not uniform, especially on  $\Sigma 3\{112\}$ -like ITBs on which Cr is enriched, Fe is depleted and Co, Ni, and Mn show local ordering. Moreover, Co and Ni share a similar periodicity, which is complementary with Mn (Fig. 1i). The ordered patterns repeat every three atomic planes, corresponding to the 9R stacking sequence. This observation is supported by line profiles of intensity taken from the EDS maps (Fig. S2). Combining the analysis of the stacking sequence, we found that Mn atoms preferentially segregate to the absolute *fcc*

stacking layer of the "...**ABC BCA CAB**..." 9R sequence (marked in bold), and Co and Ni atoms preferentially reside in the other two layers.

In addition, the atomic packing at the corners of the ridge-twin structure is more disordered, and so are the distributions of the elements. Figure 2b and 2c show the atomic structure and the corresponding EDS maps of the junctions marked by white boxes in Fig. 2a, respectively. The two areas both contain dislocation structures. At the dislocation core, Cr is enriched, and Fe, Co, Mn, and Ni are depleted at the side with tensile strain. Meanwhile, there seems to be a local ordering of certain elements along the coherent twin boundaries as marked by red arrows. For instance, in Fig. 2b, Co atoms form a pattern along the coherent boundary 1, and Co and Mn atoms form patterns along the coherent boundary 2 in Fig. 2c.

We show next that the ridge twins, with their unique structure and elemental distributions, play a distinctive role in promoting and tuning dislocation activity, thereby affecting the deformation behavior. To reveal the dynamic role of the ridge twins in plastic deformation and to best present the bulk behavior, we performed *in situ* TEM straining tests in the relatively thick samples (the thickness is above 600 nm) using the method detailed in ref. 30 to study the real-time microstructural evolution associated with the ridge-twin structure and to ensure that the results are comparable with the bulk counterpart. It was observed that the material contains very few pre-existing dislocations in the grain interior. With the application of load, dislocation activity is found at the junctions (for example, the triple junction in Fig. 1b) along  $\Sigma 3\{111\}$  CTBs (Matrix/Ridge twin-T1 boundaries) at the very beginning of plastic deformation; this is illustrated in Fig. 3a. Figure 3b and Supplementary Movie 1 show that the dislocation arrays are firstly emitted from the corner, and that these junctions act as dislocation sources that continuously emit new dislocations. Many different samples with different angles between the loading direction and the boundaries were tested to confirm that this observation was representative. There seems to be strong pinning points located at the triple junction, causing the dislocations to bow-out on the CTBs, as shown in Fig. 1b. Dislocation glide on the CTBs is not always easy, which is different from what has been usually seen in the ultra-thin TEM samples<sup>31</sup>. As shown in Fig. 3b, during dislocation motion, the pinning and de-pinning, as marked by white arrows, frequently occur such that the dislocation lines become curly. The pinning may be due to imperfections on the slip planes, which markedly slow down dislocation glide and promote complex dislocation interactions on the CTB. In addition, the dislocations on the CTBs can easily cross-slip into grains (Fig. S3), partly because the image force on these dislocations is zero as the Burgers vector is parallel to the TB<sup>31,32</sup>. In addition to the triple junctions, the  $\Sigma 3\{112\}$  ITBs can also emit partial dislocations into the grain interior. As shown in Fig. 3c, multiple types of partial dislocations can be generated from  $\Sigma 3\{112\}$  ITBs into the grains (white arrows). Combining these two scenarios, large numbers of dislocations are continuously emitted from the ridge-twin structures and spread into the interior of the twins and matrix, facilitating intense dislocation interactions and the formation of dislocation networks (Fig. S4), including deformation twinning (Fig. S5) at relatively large strains. Note that the ridge-twin structures, including the atomic structure of  $\Sigma 3\{112\}$  ITBs, remain stable during the entire deformation process. Figure 3d is a schematic illustration of the role of the ridge-twin structure in

promoting dislocation activities, which would lead to a high density of dislocations due to the relatively large number of twin-twin junctions in low-SFE HEAs.

We also investigated the role of ridge-twin structures during plastic deformation in other low-SFE materials. In the CrCoNi alloy, TWIP steel, pure Ag, and pure Cu, the ridge-twin structure is found to facilitate dislocation activities the same way as that observed in Cr<sub>20</sub>Mn<sub>14</sub>Fe<sub>26</sub>Co<sub>26</sub>Ni<sub>14</sub> TWIP HEA. For instance, in the CrCoNi alloy, the generation of dislocations from the  $\Sigma 3\{112\}$  ITBs also prevails, generating dense partial dislocations and deformation twins, as seen in Fig. 3e. Even in pure Cu, in which there is no chemical ordering, large numbers of dislocations are generated from the ridge twins (as shown by the arrows in Fig. 3f). Therefore, our broad survey demonstrates that in general the ridge-twin structure is a proficient dislocation source in all low-SFE materials.

Molecular dynamics simulations<sup>33</sup> were employed to examine the atomistic details and the formation mechanism of the ridge-twin structures. A series of metals and alloys, including Cr<sub>20</sub>Mn<sub>14</sub>Fe<sub>26</sub>Co<sub>26</sub>Ni<sub>14</sub>, CrCoNi, Cu, Ag and Al, were investigated using empirical potentials<sup>34-36</sup> (described in the Methods section). A ridge twin was constructed with the angle  $\alpha = 14^\circ$  (see illustration in Fig. 4a), followed by relaxation at 300 K and energy minimization. The obtained atomic configuration of Cr<sub>20</sub>Mn<sub>14</sub>Fe<sub>26</sub>Co<sub>26</sub>Ni<sub>14</sub> is shown in Fig. 4a (for other materials, see Fig. S6). The atoms are colored according to common neighbor analysis: blue, red and white atoms are for *fcc*, *hcp* and *other* structures, respectively. The ridge-twin structure consists of two CTBs and one ITB. As shown in Fig. 4a, every two *hcp* layers and one *fcc* layer alternate along  $\Sigma 3\{112\}$  ITB, with stacking sequence of ...ABC BCA CAB...; at the inward end of *hcp* layers, an array of  $1/6\langle 112 \rangle$  Shockley partials are formed (denoted in yellow), which are shown in the enlarged view in Fig. S7. This observation indicates the 9R-like structure of  $\Sigma 3\{112\}$  ITB is a preferable configuration, which is consistent with the experimental characterization in Fig. 1. The other materials that were studied, namely, CrCoNi, Cu and Ag (but not Al) also exhibited the 9R-like ITB (see Fig. S6).

An immediate question is why such ridge-twin structures form in low-SFE metals and alloys. To answer this question, we firstly constructed samples with alternatively regular grain boundaries (GBs), including symmetry  $\Sigma 9\{114\}$  GBs (Fig. 4b) and asymmetry  $\Sigma 9\{115\}\{111\}$  GB (Fig. 4c). The latter GB, along the same direction with that of ridge-twin structure, was heated to 900 K and annealed at that temperature for 20 ns, during which a few ridge-twin structures (as long as  $\sim 7$  nm) were seen to appear (Fig. 4d). The same scenario was observed in CrCoNi, Cu and Ag (but not Al), as shown in Fig. S8). Thus, even with for the very short simulation timescales, nano-sized ridge twins are readily formed in the metals and alloys with low-SFEs. Figure 4e compares the interfacial energy,  $\gamma_{\text{RTWIN}}$ , of the ridge-twin structure ( $2*\Sigma 3\{111\}$  CTBs +  $\Sigma 3\{112\}$  ITB) with the regular grain boundaries ( $\Sigma 9\{114\}$  and  $\Sigma 9\{115\}\{111\}$ ) energy (as detailed in Methods). Apparently, ridge-twin structures are more energetically favored, which is consistent with the structural evolution observed in Fig. 4d and Fig. S8 for the Cr<sub>20</sub>Mn<sub>14</sub>Fe<sub>26</sub>Co<sub>26</sub>Ni<sub>14</sub>, CrCoNi, Cu and Ag materials. Note that the ratios of  $\Sigma 3\{112\}$  ITB to  $\Sigma 9\{114\}$  GB energies and  $\Sigma 9\{114\}$  GB to  $\gamma_{\text{RTWIN}}$  energies scale linearly with the twin boundary energy (TBE) as well as SFE for all the studied materials

(Fig. S9). This suggests that the TBE or SFE is the critical factor responsible for the energetic preference of the ridge-twin structure. As a result, low-SFE materials are prone to the formation of ridge twins, and vice versa. Moreover, the measured  $\gamma_{\text{RTWIN}}$  is plotted in Fig. 4f as a function of various angles  $\alpha$ , where it is evident that the minimum value of  $\gamma_{\text{RTWIN}}$  is located at  $\alpha \approx 14^\circ$  for  $\text{Cr}_{20}\text{Mn}_{14}\text{Fe}_{26}\text{Co}_{26}\text{Ni}_{14}$ , Ag and Cu, as shown in Fig. S10. Such characteristic angles (around  $14^\circ$ ) of ridge twins are close to that seen in the TEM observations in Fig. 1. As shown in Fig. 4g, the ridge-twin structure interfacial energy,  $\gamma_{\text{RTWIN}}$ , is also dependent on the length of the twin: the longer the ridge twin, the smaller the  $\gamma_{\text{RTWIN}}$ . Ostwald-Ripening-like behavior would therefore be expected, in that a larger ridge twin would be energetically favored to grow at the expense of smaller ones.

As discussed above, the atomic structure of the ridge twins is unique, consisting of 9R-like structure and array of partial dislocations. Figure S11 presents the stress field of ridge twins in pure Ag, showing the distributions of pronounced hydrostatic stress ( $\sigma_{\text{hydro}}$ ) and shear stress ( $\tau_{xz}$ ). Along  $\Sigma 3\{112\}$  ITB, the hydrostatic stress oscillates with the repeating pattern, 5 GPa, 0 GPa and -5 GPa, while the corresponding shear stress alternates with  $\sim 2$  GPa, 0 GPa and  $\sim -2$  GPa. Such unique structures and properties should influence the mechanical deformation. Accordingly, we implemented the MD simulation to investigate the tensile deformation (in the  $x$  direction defined in Fig. 4) of  $\text{Cr}_{20}\text{Mn}_{14}\text{Fe}_{26}\text{Co}_{26}\text{Ni}_{14}$  alloy containing the ridge twins, as shown in Fig. S12. At a tensile strain of 4%, a Shockley partial begins to emit from the corner of a ridge twin and propagate to the surface. With increasing strain, more and more Shockley partials are generated and emitted from  $\Sigma 3\{112\}$  ITB, leaving defects to influence subsequent deformation. These observations are well consistent with our TEM characterization in Fig. 3 and demonstrate the critical role of ridge twins as proficient dislocation sources that would markedly influence the ensuing plastic deformation.

In summary, ridge twins that frequently form during materials preparation or processing to accommodate the twin-twin architectures are found to be unique structural defects in low-SFE materials with energy advantages over other types of grain and twin boundaries. The ridged structures act as an important nucleation source of dislocations, promoting their activity and interactions to influence plasticity. As a final note, in compositionally complex alloys with multiple principal elements and low SFEs, the distribution of elements on these ridge-twin boundaries and at the twin-twin junctions may exhibit local chemical ordering, which alters the local environment for dislocation nucleation and glide. Further study is necessary to fully understand the effects associated with such chemical heterogeneity at these locations and whether such local ordering could be utilized to tune dislocation behavior in alloys.

## References

- [1] De Cooman, B. C., Estrin, Y., Kim, S. K. Twinning-induced plasticity (TWIP) steels. *Acta Mater.* **142**, 283-362 (2018).
- [2] Bouaziz, O., Allain, S., Scott, C. P., Cugy, P., Barbier, D. High manganese austenitic twinning induced plasticity steels: A review of the microstructure properties relationships. *Curr. Opin. Solid State Mat. Sci.*

15, 141-168 (2011).

- [3] Liang, Z. Y., Li, Y. Z., Huang, M. X. The respective hardening contributions of dislocations and twins to the flow stress of a twinning-induced plasticity steel. *Scr. Mater.* **112**, 28-31 (2016).
- [4] Fu, X., Wu, X., Yu, Q. Dislocation plasticity reigns in a traditional twinning-induced plasticity (TWIP) steel by in situ observation. *Mater. Today Nano* **3**, 48-53 (2018).
- [5] Grässel, O., Krüger, L., Frommeyer, G., Meyer, L. W. High strength Fe-Mn-(Al, Si) TRIP/TWIP steels development - properties - application. *Int. J. Plast.* **16**, 1391-1409 (2000).
- [6] Frommeyer, G., Brüh, U., Neumann, P. Supra-ductile and high-strength manganese-TRIP/TWIP Steels for high energy absorption purposes. *ISIJ Int.* **43**, 438-446 (2003).
- [7] Deng, Y. et al. Design of a twinning-induced plasticity high entropy alloy. *Acta Mater.* **94**, 124-133 (2015).
- [8] Karaman, I. et al. Modeling the deformation behavior of Hadfield steel single and polycrystals due to twinning and slip. *Acta Mater.* **48**, 2031-2047 (2000).
- [9] Lu, K., Lu, L., Suresh, S. Strengthening materials by engineering coherent internal boundaries at the nanoscale. *Science* **324**, 349-352 (2009).
- [10] Venables, J. A. Deformation twinning in face-centred cubic metals. *Philos. Mag.* **6**, 379-396 (1961).
- [11] Mahajan, S., Chin, G. Y. Formation of deformation twins in f.c.c. crystals. *Acta Metall.* **21**, 1353-1363 (1973).
- [12] Christian, J. W., Mahajan, S. Deformation twinning. *Prog. Mater. Sci.* **39**, 1-157 (1995).
- [13] Husser, E., Bargmann, S. Modeling twinning-induced lattice reorientation and slip-in-twin deformation. *J. Mech. Phys. Solids* **122**, 315-339 (2019).
- [14] Asgari, S., El-Danaf, E., Kalidindi, S. R., Doherty, R. D. Strain hardening regimes and microstructural evolution during large strain compression of low stacking fault energy fcc alloys that form deformation twins. *Metall. Mater. Trans. A*, **28**, 1781-1795 (1997).
- [15] Lu, L., Chen, X., Huang, X., Lu, K. Revealing the maximum strength in nanotwinned copper. *Science* **323**, 607-610 (2009).
- [16] Beladi, H. et al. Orientation dependence of twinning and strain hardening behaviour of a high manganese twinning induced plasticity steel with polycrystalline structure. *Acta Mater.* **59**, 7787-7799 (2011).
- [17] Rémy, L. Twin-slip interaction in f.c.c. crystals. *Acta Metall.* **25**, 711-714 (1977).

- [18] Li, X., Wei, Y., Lu, L., Lu, K., Gao, H. Dislocation nucleation governed softening and maximum strength in nano-twinned metals. *Nature* **464**, 877-880 (2010).
- [19] Taheri Mousavi, S. M., Zhou, H., Zou, G., Gao, H. Transition from source- to stress-controlled plasticity in nanotwinned materials below a softening temperature. *npj Comput. Mater.* **5**, 2 (2019).
- [20] Wang, Y. B., Sui, M. L., Ma, E. In situ observation of twin boundary migration in copper with nanoscale twins during tensile deformation. *Philos. Mag. Lett.* **87**, 935-942 (2007).
- [21] Chen, S. et al. Real-time observations of TRIP-induced ultrahigh strain hardening in a dual-phase CrMnFeCoNi high-entropy alloy. *Nat. Commun.* **11**, 826 (2020).
- [22] Ranganathan, S. On the geometry of coincidence-site lattice. *Acta Crystallogr.* **21**, 197-199 (1966).
- [23] Randle, V. Twinning-related grain boundary engineering. *Acta Mater.* **52**, 4067-4081 (2004).
- [24] Randle, V., Coleman, M., Waterton, M. The Role of  $\Sigma 9$  Boundaries in Grain Boundary Engineering. *Metall. Mater. Trans. A* **42**, 582-586 (2011).
- [25] Liu, L., Wang, J., Gong, S. K., Mao, S. X. High resolution transmission electron microscope observation of zero-strain deformation twinning mechanisms in Ag. *Phys. Rev. Lett.* **106**, 175504 (2011).
- [26] Wang, J., Anderoglu, O., Hirth, J. P., Misra, A., Zhang, X. Dislocation structures of  $\Sigma 3$  {112} twin boundaries in face centered cubic metals. *Appl. Phys. Lett.* **95**, 021908 (2009).
- [27] Lucadamo, G., Medlin, D. L. Geometric Origin of Hexagonal Close Packing at a Grain Boundary in Gold. *Science* **300**, 1272-1275 (2003).
- [28] Ernst, F. et al. Theoretical prediction and direct observation of the 9R structure in Ag. *Phys. Rev. Lett.* **69**, 620-623 (1992).
- [29] Wolf, U., Ernst, F., Muschik, T., Finnis, M. W., Fischmeister, H. F. The influence of grain boundary inclination on the structure and energy of  $\sigma = 3$  grain boundaries in copper. *Philos. Mag. A* **66**, 991-1016 (1992).
- [30] Zhang, Z. et al. Nanoscale origins of the damage tolerance of the high-entropy alloy CrMnFeCoNi. *Nat. Commun.* **6**, 10143 (2015).
- [31] Zhang, Z. et al. Dislocation mechanisms and 3D twin architectures generate exceptional strength-ductility-toughness combination in CrCoNi medium-entropy alloy. *Nat. Commun.* **8**, 14390 (2017).
- [32] Priester, L., Khalfallah, O. Image force on a lattice dislocation due to a grain boundary in anisotropic f.c.c. materials. *Philos. Mag. A* **69**, 471-484 (1994).

- [33] Plimpton, S. Fast parallel algorithms for short range molecular dynamics. *J. Comput. Phys.* **117**, 1–19 (1995).
- [34] Choi, W. M., Jo, Y. H., Sohn, S. S., Lee, S., Lee, B.-J. Understanding the physical metallurgy of the CoCrFeMnNi high-entropy alloy: an atomistic simulation study. *npj Comput. Mater.* **4**, 1 (2018).
- [35] Li, Q. J., Sheng, H., Ma, E. Strengthening in multi-principal element alloys with local-chemical-order roughened dislocation pathways. *Nat. Commun.* **10**, 3563 (2019).
- [36] Sheng, H. W., Kramer, M. J., Cadien, A., Fujita, T., Chen, M. W. Highly optimized embedded-atom-method potentials for fourteen fcc metals. *Phys. Rev. B* **83**, 134118 (2011).

## Methods

**Alloys processing.** The  $\text{Cr}_{20}\text{Mn}_{14}\text{Fe}_{26}\text{Co}_{26}\text{Ni}_{14}$  TWIP HEA for this study were produced from pure metals with a purity better than 99.8% which were arc-melted in a vacuum induction furnace. The as-produced ingots were then processed to obtain a fully crystallized microstructure in the same way as that of Cantor alloy reported in a recent paper<sup>21</sup>. The equiatomic CrCoNi medium-entropy alloy<sup>37</sup> and TWIP steel<sup>4</sup> was synthesized as reported in the previous papers. The pure metals investigated used the commercial annealed Cu and Ag with purity better than 99.5%.

### TEM sample preparation and microstructural characterization.

#### 1) SEM sample preparation for three-dimensional observation

The sample were cut into 1.5 mm slices, and then were ground and mechanical polished to obtain flat and clean surface. The three-dimension morphology of the twin architecture was acquired using a “cut and see” method in a high-performance Hitachi NX9000 microscope, in which SEM column and FIB column were orthogonally arranged to eliminate aspect deformation and any shift of the field of view. The sample was sliced layer-by-layer using FIB with a step size of 20 nm and the images of the cross-section in every slice were acquired using SEM.

#### 2) TEM sample preparation

Specimens for TEM characterization were first sectioned from the alloy plates to 500  $\mu\text{m}$  using electric discharge machining. The as-sectioned samples were milled and polished with SiC papers down to thickness of 60  $\mu\text{m}$ , and then punched into discs with diameter of 3 mm. The TWIP HEA and CrCoNi discs were further thinned using twin-jet electrochemical polishing in a solution of 6% perchloric acid, 34% butanol and 60% methanol at -30 °C and 12 V to obtain electron-transparent thin foils. The polished foils were rinsed immediately in ethanol. TEM thin foils of pure Cu and Ag were prepared by  $\text{Ar}^+$ -ion milling at accelerating voltage of 5 kV, 3 kV and 1 kV.

#### 3) TEM characterization and EDS analysis

Characterization of morphology of ridge twins was performed by bright field TEM imaging in a FEI Tecnai G2 F20 microscope operating at 200 kV. The atomic structure was acquired by using high-angle annular dark field (HAADF) scanning transmission electron microscopy (STEM) in spherical aberration corrected microscopes (FEI, Titan G<sup>2</sup> 80-200 ChemiSTEM and STEM, Titan Cubed Themis G<sup>2</sup> 300). The atomic-resolution EDS mapping was acquired using Thermo Fisher Scientific Ultra-X EDS in the Spectra Ultra with CEOS DCOR probe aberration corrector microscope operating at 200 kV with a 50 mm C2 aperture. The beam current was set to roughly 100 pA, with the dwell time of 20 ms. A complete process of EDS mapping took about half an hour to obtain a high signal-to-noise ratio without incurring damage to the sample.

#### 4) *In situ* TEM straining tests

The TEM specimens with a diameter of 3 mm were used for *in situ* TEM straining tests. The TEM samples were attached to 11.5 mm × 2.5 mm × 0.5 mm stainless steel substrates, which were processed as narrow windows for transmission of the electron beam. Only samples that were well attached to the substrate and free of contamination from the sample preparation, were selected for *in situ* TEM straining tests. *In situ* tensile tests in the TEM were conducted with a Gatan model 671 single-tilt holder in the FEI Tecnai G<sup>2</sup> F20 microscope. Tensile loading was accomplished by applying intermittent displacement pulses manually, with a displacement rate of ~1 μm/s. Observation of the dislocation behavior was performed at the holding period between pulses. Regions ~10 mm away from the hole, which were hundreds of micrometers thick but still electron-transparent, were monitored during the straining process to acquire results comparable with those from bulk samples.

### Computation simulations

#### 1) Atomic configurations setup

Molecular dynamics (MD) simulations of Cr<sub>20</sub>Mn<sub>14</sub>Fe<sub>26</sub>Co<sub>26</sub>Ni<sub>14</sub>, CrCoNi, Ag, Cu and Al were performed using the software package LAMMPS<sup>33</sup> with the empirical EAM potentials<sup>34-36</sup>. The configurations of the ridge twin structure (Fig. 4a), Σ9{114} grain boundaries (Fig. 4b) and Σ9{115}{111} grain boundary (Fig. 4c) were first constructed, followed by relaxation at 300 K and energy minimization. The simulation cells were originally set as , and for the x, y and z directions, respectively. A variety of sizes of ridge-twin structures were constructed for further analysis. Two kinds of boundary conditions were applied: (i) periodic boundary condition (PBC) for z direction and free surfaces for x and y directions (*e.g.*, Fig. 4a-d, Fig. S6-8); (ii) PBC for x and z directions, while free surface for y direction (*e.g.*, Fig. S11, S12). The software of OVITO was used to display the configurations of atoms colored according to common neighbor analysis<sup>38</sup>. The partial dislocations were identified by the dislocation extraction (DXA) method<sup>38</sup>.

#### 2) High temperature annealing

The atomic configurations for  $\text{Cr}_{20}\text{Mn}_{14}\text{Fe}_{26}\text{Co}_{26}\text{Ni}_{14}$ , CrCoNi, Ag, Cu and Al, with asymmetry  $\Sigma 9\{115\}$   $\{111\}$  grain boundary (Fig. 4c) were heated to 900 K through the isothermal–isobaric (NPT) ensemble under a Nose-Hoover thermostat with zero external pressure. These samples were annealed at 900 K for 20 ns and then underwent energy minimization for structural analysis.

### 3) Calculation of interfacial energies

The interfacial energies ( $\gamma$ ) of the grain boundaries (e.g.,  $\Sigma 9\{114\}$ ,  $\Sigma 9\{115\}\{111\}$  and  $\Sigma 3\{112\}$ -like) as well as stacking fault energy (SFE) and coherent twin boundary energy (TBE) were calculated by:

$$\gamma = \frac{E - E_0}{S}$$

where  $E$  is the total potential energy for  $N$  atoms within 3 nm of the interface of interest,  $E_0$  is the potential energy for  $N$  atoms in a perfect crystal lattice, and  $S$  is the area of the interface. The interfacial energy of ridge-twin structure,  $\gamma_{\text{RTWIN}}$ , was calculated according to potential energy of the atoms involved with the ridge twins, whereas  $S$  was the projected area of the ridge-twin onto the  $\{111\}$  plane (e.g., the horizontal

area in Fig. 4a). Note that the interfacial energies ( $\gamma$ ) of the grain boundaries (e.g.,  $\Sigma 9\{114\}$ ,  $\Sigma 9\{115\}\{111\}$  and  $\Sigma 3\{112\}$ -like) were calculated only for the middle portion of these boundaries in order to avoid the effect of the triple junction, corner or free surface. For  $\text{Cr}_{20}\text{Mn}_{14}\text{Fe}_{26}\text{Co}_{26}\text{Ni}_{14}$  and CrCoNi, a total of 500 independent configurations was calculated for each interface and averaged to achieve convergence.

### 4) Tensile deformation of ridge twins

A sample of  $\text{Cr}_{20}\text{Mn}_{14}\text{Fe}_{26}\text{Co}_{26}\text{Ni}_{14}$  with a ridge-twin structure was deformed in tension. The dimensions of this sample were  $\sim 60$  nm in the  $x$  direction,  $\sim 54$  nm in the  $y$  direction and 10 nm in the  $z$  direction, with a periodic boundary condition in the  $x$  and  $z$  directions and a free surface in the  $y$  direction. Uniaxial tensile deformation along the  $x$  axis was applied at a strain rate of  $10^{-5}$  /ps at 300 K. For the results shown in Fig. 4, only non-*fcc* atoms are colored (orange for *hcp* atoms and purple for *other* atoms) to identify the microstructure involved with the deformed ridge twin.

### Data availability

All data generated or analysed during this study are included in the published article and Supplementary information, and are available from the corresponding authors upon reasonable request.

### References

[37] Gludovatz B, Hohenwarter A, Thurston K V S, et al. Exceptional damage-tolerance of a medium-entropy alloy CrCoNi at cryogenic temperatures. *Nat. Commun.* **7**, 10602 (2016).

[38] Stukowski A. Visualization and analysis of atomistic simulation data with OVITO – the Open Visualization Tool. *Model. Simul. Mater. Sci. Eng.* **18**, 015012 (2010).

## Declarations

### Acknowledgments

This work was funded by Natural Science Foundation of China 51871197, the National 111 Project under grant no. B16042 and the State Key Program for Basic Research in China under grant no. 2017YFA0208200. ROR was supported by the U.S. Department of Energy, Office of Science, Basic Energy Sciences, Materials Sciences and Engineering Division under contract no. DE-AC02-CH11231. J.D. and E.M. acknowledge XJTU for hosting their research at the Center for Alloy Innovation and Design (CAID).

### Author Contributions

Q.Y. and J.D. designed the research. X.F., Q.Y., C.K., Y.C., Y.F., and Y.G. performed STEM, EDX and *in situ* experiments. E.P. synthesized alloys. J.D. performed theoretical modelling and ab initio simulations. Z.Z., Q.Y., J.D., E.M. and R.R. contributed to data analysis and discussions. Q.Y., J.D., R.R., and E.M. wrote the paper.

### Competing Interests

The authors declare no competing interests.

### Additional Information

Supplementary information is available for this paper.

### Corresponding authors

Correspondence and request for materials should be addressed to Jun Ding ([dingsn@xjtu.edu.cn](mailto:dingsn@xjtu.edu.cn)), Robert O. Ritchie ([roritchie@lbl.gov](mailto:roritchie@lbl.gov)), En Ma ([maen@xjtu.edu.cn](mailto:maen@xjtu.edu.cn)), or Qian Yu ([yu\\_qian@zju.edu.cn](mailto:yu_qian@zju.edu.cn))

## Figures

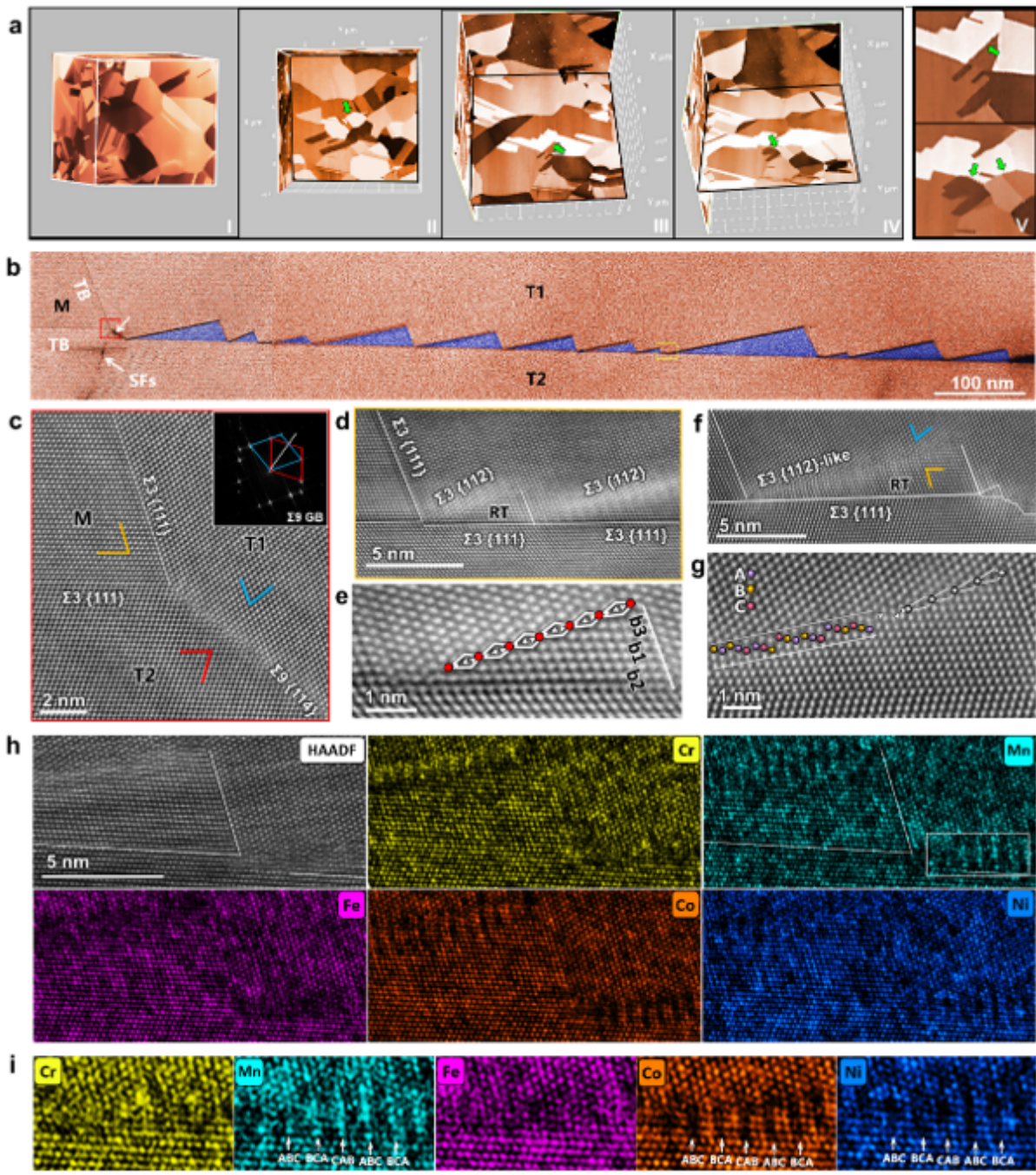
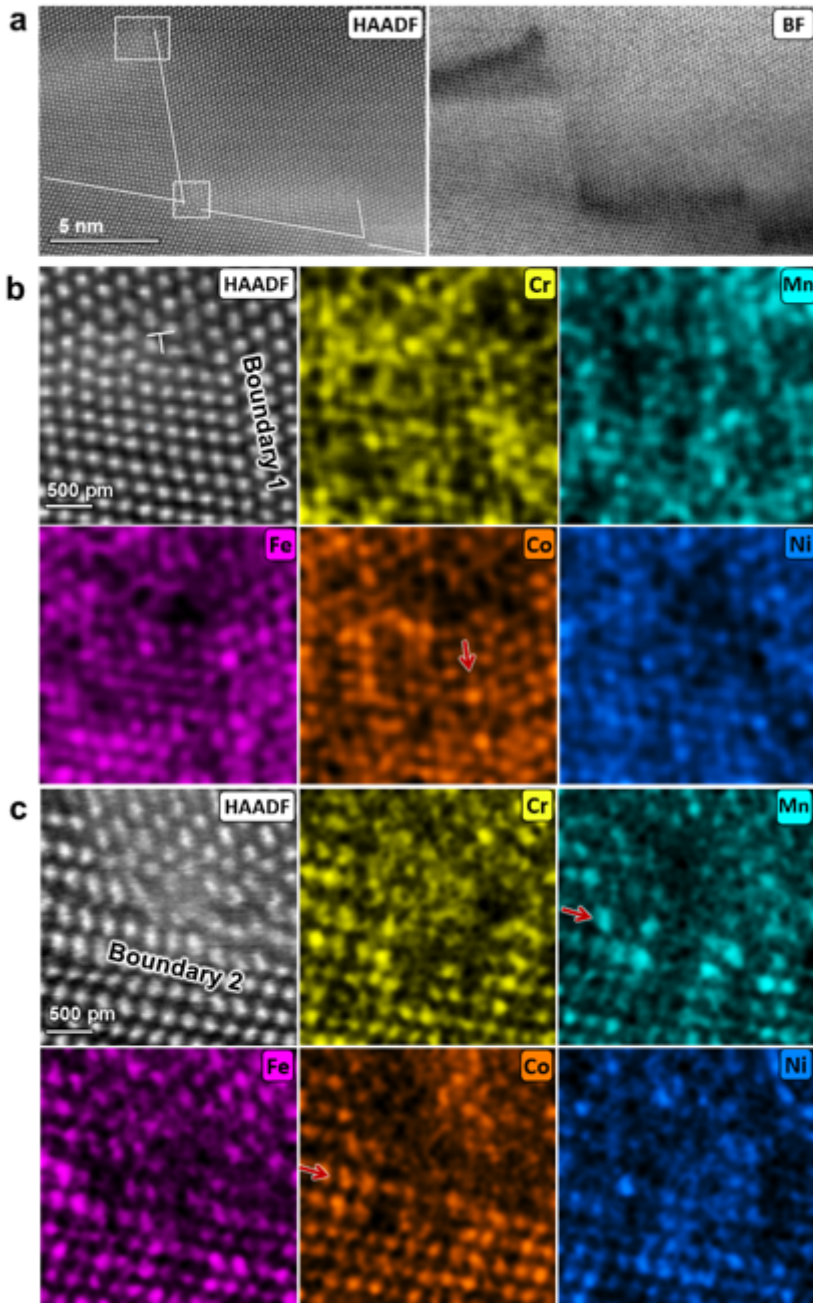


Figure 1

**Twin boundary structure in  $\text{Cr}_{20}\text{Mn}_{14}\text{Fe}_{26}\text{Co}_{26}\text{Ni}_{14}$  TWIP HEA.** (a) Twin architecture viewed by using the “cut & see” method. SEM images I-IV are views from different angles; image V shows the enlarged view of the serrated TBs in images III and IV, which are labelled by green arrows. (b) The stitching STEM bright field image showing a complex boundary at the intersection of Matrix (M), Twin1 (T1) and Twin2 (T2). The complex boundary contains one segment of a ~10 nm long boundary, followed by a string of triangular boundaries. (c) Atomic structure of the twin-twin intersection in the area marked by the red box in b and the corresponding FFT pattern of T1 and T2. (d) Atomic structure on a typical triangular boundary in the area marked by the yellow box in b, showing the ridge-twin structure. (e) Enlarged image

of the ridge twin (labelled as RT) in **d** showing the dislocation array on ridge twin-T1 ITB with a sequence of  $b_2: b_1: b_3$ , the same as  $\Sigma 3\{112\}$  ITBs. **(f)** A ridge twin with a  $\Sigma 3\{112\}$ -like ITB whose structure is different from the typical  $\Sigma 3\{112\}$  ITBs. **(g)** Enlarged image of the ridge twin in **f** showing a deflected structure. **(h)** Atomic-resolution HAADF image of a ridge twin and the corresponding energy-dispersive X-ray spectroscopy (EDS) maps for individual elements of Cr, Mn, Fe, Co, and Ni, taken with  $\langle 110 \rangle$  zone axis. The white lines marked out the CTBs. **(i)** Enlarged view of the EDS maps of the five elements along ITB denoted by the white box in **h**, showing the local ordering.



**Figure 2**

**Atomic structure and element distribution at the junctions of the ridge twin.** **(a)** Atomic-resolution STEM HAADF and bright field (BF) images of a ridge twin, taken with  $\langle 110 \rangle$  zone axis. **(b)** HAADF image

showing the structure of a CTB-ITB corner and the corresponding EDS maps for individual elements of Cr, Mn, Fe, Co, and Ni. (c) HAADF image showing the structure at the location connecting two ridge twins and the corresponding EDS maps for Cr, Mn, Fe, Co, and Ni. The local ordering of certain elements along the CTBs are pointed out using red arrows.

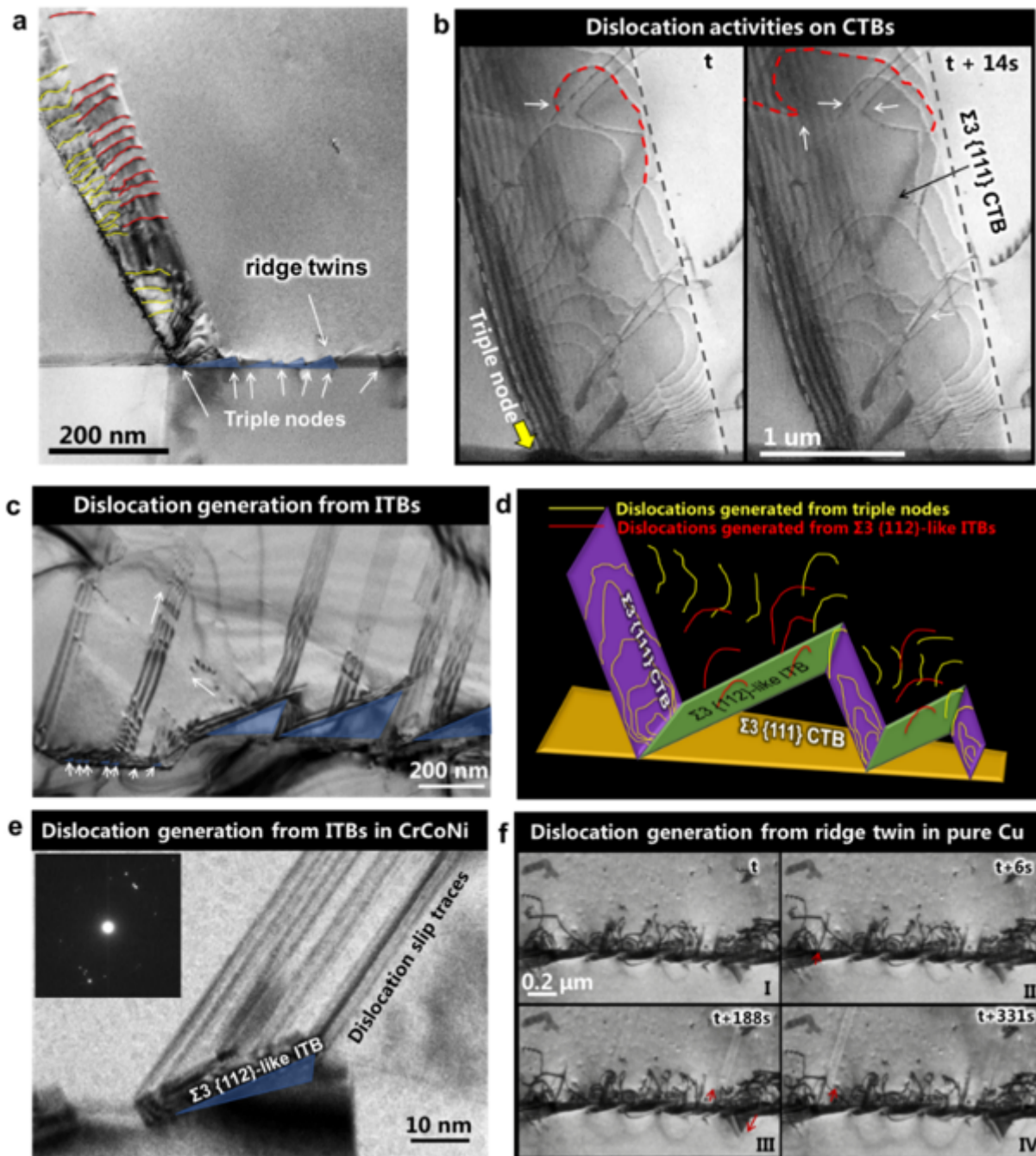
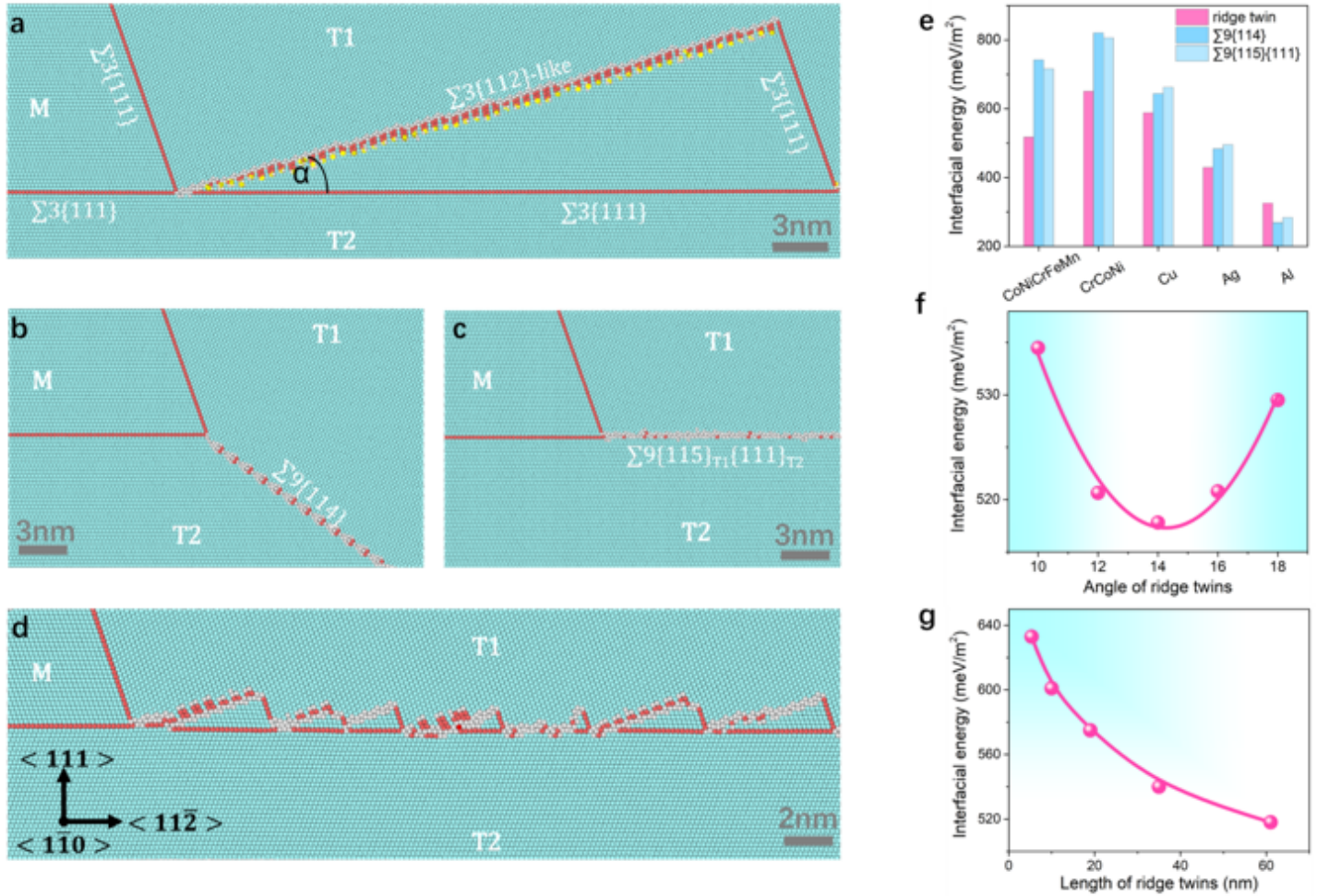


Figure 3

**Dislocation generation from the ridge-twin structure.** (a) Bright field STEM image showing dislocation arrays launched from triple-TBs node in 1b as the sample was deformed. (b) Serial TEM images captured during *in situ* TEM straining tests showing dislocation generation from the triple junction and the further

sluggish motion on the CTB. The triple junction is marked with a yellow arrow. (c) Bright field image showing dislocation arrays generated from  $\Sigma 3\{112\}$ -like ITB of ridge-twin boundary in TWIP HEA. (d) Schematic illustration of the role of the ridge-twin structure in promoting dislocation activity. (e) Bright field image showing dislocation arrays and deformation twinning generated from a ridge twin in the equiatomic CrCoNi alloy. (f) Serial images showing dislocations generated from the ridge twins in pure Cu.



**Figure 4**

**MD simulation of the ridge-twin structure in  $\text{Cr}_{20}\text{Mn}_{14}\text{Fe}_{26}\text{Co}_{26}\text{Ni}_{14}$  alloy.** (a) Atomic configuration of the ridge-twin structure (combination of  $\Sigma 3\{112\}$  ITB, two of  $\Sigma 3\{111\}$  CTBs) with the angle  $\alpha = 14^\circ$ . The atoms are colored according to common neighbor analysis: blue, red and white atoms represent *fcc*, *hcp* and *other* structures, respectively. An array of  $1/6\langle 112 \rangle$  Shockley partials (in yellow) are denoted. (b) and (c) show the atomic configuration with the grain boundary of  $\Sigma 9\{114\}$  and  $\Sigma 9\{115\}_{T1}\{111\}_{T2}$ , respectively. (d) The atomic configuration of  $\Sigma 9\{115\}_{T1}\{111\}_{T2}$  boundary after the annealing at 900 K. (e) The interfacial energy of the ridge twin boundary as well as  $\Sigma 9\{114\}$  and  $\Sigma 9\{115\}_{T1}\{111\}_{T2}$  (denoted in (b) and (c), respectively) for  $\text{Cr}_{20}\text{Mn}_{14}\text{Fe}_{26}\text{Co}_{26}\text{Ni}_{14}$ , CrCoNi, Ag, Cu and Al. (f) and (g) respectively show the

calculated interfacial energies of ridge twins at various angles and lengths for  $\text{Cr}_{20}\text{Mn}_{14}\text{Fe}_{26}\text{Co}_{26}\text{Ni}_{14}$  alloy.

## Supplementary Files

This is a list of supplementary files associated with this preprint. Click to download.

- [YuQiantwipheaSI20220322.docx](#)
- [Movie1dislocationonCTB5timespeedup.wmv](#)